https://doi.org/10.5194/egusphere-2026-1852
Preprint. Discussion started: 18 May 2026

A high-resolution, submesoscale-resolving ocean model of South East Queensland (ROMS v4.2).

David E. Gwyther[1], Megan Jeffers[1], and Helen Bostock[1]

[1]School of the Environment, The University of Queensland, St Lucia, QLD, Australia

Correspondence: David E. Gwyther (david.gwyther@gmail.com)

Abstract. The ocean exhibits a continuum of motions spanning basin-scale circulation to micro-scale turbulence where between mesoscale eddies and small-scale turbulence lies the submesoscale (~0.1-10 km, hours-days). The submesoscale is characterised by fronts, filaments and small coherent vortices that arise from instabilities of mesoscale currents, interactions with topography, and buoyancy forcing. These processes restratify the upper ocean while simultaneously enhancing vertical tracer exchange through intense vertical velocities concentrated at density gradients. In the East Australian Current, the western boundary current of the South Pacific Gyre, the jet accelerates and interacts with the continental shelf off South East Queensland, creating conditions favourable for submesoscale activity. Yet these processes remain unresolved and unexplored in existing regional simulations: mesoscale regional models do not resolve energetic frontal processes, high-resolution coastal models lack realistic offshore forcing, and observations alone are insufficient to constrain the three-dimensional subsurface circulation. Here, we present a submesoscale-permitting implementation of the Regional Ocean Modelling System (ROMS v4.2) for the EAC jet intensification region offshore of South East Queensland and northern New South Wales, Australia. We demonstrate that our model generates energetic fronts and filaments along the continental shelf edge, while maintaining surface and subsurface mesoscale hydrographic structure consistent with observations. Relative to mesoscale-resolving simulations, the configuration exhibits substantially increased hotspots of divergence, vorticity and vertical velocity variance, together with a flatter kinetic energy spectrum indicative of resolved submesoscale dynamics. A demonstration of the continental shelf break in the vicinity of K'gari shows the accelerating jet interacting with coastal promontories and the shelf break, producing localised and persistent submesoscale activity. This configuration enables investigation of submesoscale emergence and interaction with the mesoscale circulation, including jet-shelf modification, cross-shelf exchange and energy transfer across scales. This approach provides a pathway to quantify energy pathways and ocean dynamics, with applications extending beyond the East Australian Current to other western boundary current systems.

1 Introduction

The ocean flows with a hierarchy of multi-scale motion, from large basin-scale gyres, to mesoscale eddies and the finer, rapidly evolving submesoscale (McWilliams, 2016). The submesoscale is characterised by its small spatial extent and transient, chaotic behaviour (McWilliams, 2019). While large-scale and mesoscale features can be observed from satellite and inferred from long-term monitoring, sustained observations of submesoscale processes remain challenging, leading to large unknowns.

https://doi.org/10.5194/egusphere-2026-1852
Preprint. Discussion started: 18 May 2026

Yet, submesoscale processes play a critical role in driving divergent horizontal flow and strong vertical currents. This has implications for heat exchange (e.g. Klein and Lapeyre, 2009; Su et al., 2018) and nutrient transport (e.g. Kessouri et al., 2020). Despite their importance, submesoscale dynamics have received limited observational focus, and most numerical modelling studies prioritise capturing mesoscale features without the spatial resolution required to resolve smaller-scale physics.

Submesoscale currents are characterised by horizontal spatial scales of $\mathcal{O}(10\ \mathrm{m} - 10\ \mathrm{km})$, vertical spatial scales of $\mathcal{O}(10\ \mathrm{m} - 100\ \mathrm{m})$ and evolutionary time scales of hours to days (McWilliams, 2019). Common submesoscale features include eddies (rotating bodies of water), filaments (narrow regions of horizontal strain and extension) and fronts (sharp horizontal gradients in water properties). Submesoscale motions arise through several mechanisms including: extraction of available potential energy from background density gradients; vorticity generation via topographic drag; as well as boundary current separation and wake instability (McWilliams, 2019). These processes disrupt the hydrostatic and/or geostrophic balance, leading to the formation of dynamic, small-scale features and driving a turbulent energy cascade towards even smaller scales. Submesoscale flows are fundamentally defined by Rossby numbers of order unity ($\mathrm{Ro} \sim \mathcal{O}(1)$), indicating that the advective acceleration is as important as the Coriolis acceleration, and therefore the flow is not close to geostrophic balance. In addition, submesoscale dynamics are further indicated by relative vorticity (spatial variation of velocity) that is comparable to the planetary vorticity ($\zeta/f \sim \mathcal{O}(1)$); large horizontal strain rates leading to rapid sharpening of density gradients; significant horizontal divergence associated with overturning circulation; as well as strong and intermittent vertical velocities.

The East Australian Current (EAC), the western boundary current of the South Pacific Gyre, strongly influences ocean conditions, weather and climate along Australia's populous east coast (Oke et al., 2019), as well as nutrient upwelling and biological productivity (Everett et al., 2012). The EAC forms as westward-flowing jets from the South Pacific Ocean encounter the continental shelf off Queensland. The North Caledonian Jet bifurcates at 18°S, with the southern deflection flowing along the continental shelf and forming the beginning of a coherent western boundary current - the EAC (Ridgway and Dunn, 2003). At ∼22°S, the westward-flowing South Caledonian Jet enters the EAC, further strengthening this western boundary current. As this coherent jet flows southward towards the northeastern tip of K'gari (formerly Fraser Island) at ∼25°S, it moves onto the shallower and narrower continental slope, concurrently the jet accelerates, narrows and deepens (Ridgway and Dunn, 2003). This intensification region is a critical dynamic zone: the energy of the coherent jet through this region sets the downstream oceanic conditions throughout the Tasman Sea (e.g. Li et al., 2021; Gwyther et al., 2022), while variability in the jet influences the distribution of heat, nutrients and marine ecosystems through changes to cross-shelf exchange (Malan et al., 2023). Despite its dynamical significance, the jet intensification region has received only limited dedicated observational or modelling attention (Ridgway and Dunn, 2003; Sloyan et al., 2024), leaving key aspects of its dynamics, especially the details of submesoscale-mesoscale interactions, under-researched in this important zone. Furthermore, with the EAC system being projected to shift southwards (e.g. Cetina-Heredia et al., 2014) with enhanced eddy activity (Li et al., 2022), understanding the drivers and impacts of this system are critically important.

The EAC exhibits a wide range of mesoscale dynamics, including seasonal heat transport (Sobral et al., 2024), jet instability (Archer et al., 2017), eddy formation and propagation (Li et al., 2021), eddy-mean flow interactions (Macdonald et al., 2013) and cross-shelf exchange (Malan et al., 2020). Like other dynamic ocean regions, it also exhibits strong submesoscale activity, though these have received far less research attention. Submesoscale eddies and filaments have been observed in the region (Mantovanelli et al., 2017; Archer et al., 2020), and their effects on biomass and primary productivity have been investigated (Mullaney and Suthers, 2013; Bourg et al., 2024; Chapman et al., 2024). The contribution of submesoscale processes in spatial heat advection (Baird and Ridgway, 2012) as well as vertical transport of heat and biomass (Azaneu et al., 2026) in the eddy-dominated regions south of the EAC separation zone have also been demonstrated. Yet, no studies have yet examined the prevalence and significance of submesoscale processes in the most energetic, jet intensification region, leaving a substantial knowledge gap in understanding their broader influence on the EAC system.

Numerous studies have demonstrated the importance of high resolution models for resolving submesoscale processes (e.g. Capet et al., 2008; Zhong and Bracco, 2013; Soufflet et al., 2016), yet capturing these dynamics within a data-assimilating simulation remains challenging (Kerry et al., 2020), and reliant on high-resolution data streams (Kerry et al., 2026). Moreover, it has been suggested that increasing model resolution to capture the submesoscale can reduce the ability of the data assimilation system to achieve skilful prediction of the mesoscale evolution (Sandery and Sakov, 2017). In this study we introduce a new high-resolution numerical ocean model of the EAC jet intensification zone, designed to answer key questions about how submesoscale processes influence the oceanography of the EAC and the continental shelf region of South East Queensland and Northern New South Wales. In Section 2, the model configuration is described, followed by an evaluation of model performance in Section 3. In Section 4, a brief overview and interpretation of submesoscale dynamics are presented, demonstrating the performance of this model for simulating these processes. Section 5 summarises and concludes with model issues, key discussion points, and future development and applications for this simulation.

2 Model description

2.1 High-resolution South East Queensland ROMS

We use the Regional Ocean Modelling System (ROMS v4.2; Shchepetkin and McWilliams, 2005), a free-surface, hydrostatic, primitive equation model, that employs a terrain-following *s*-coordinate (Song and Haidvogel, 1994). ROMS is widely-used for simulating coastal, shelf and near-shelf processes in regional applications. It has been previously used to simulate the EAC along the south-east coast of Australia (e.g. Kerry et al., 2016), as well as other locations around the Australian continental shelf (e.g. Janeković et al., 2022; Aijaz et al., 2024). ROMS has also previously been used to simulate submesoscale processes in many different regions, for example, in the Baltic Sea (Onken et al., 2020), for the Hawaiʻian Islands (Friedrich et al., 2024), southern Indian Ocean (Zhou et al., 2024) and the South China Sea (Lin et al., 2020).

For the Southeast Queensland ROMS (SEQld ROMS) we configure the vertical stretching parameters over the 31 vertical layers to provide enhanced vertical resolution near the surface- and bottom-boundary layers, using the transformation and stretching functions `Vtransform = 2` and `Vstretching = 4`. With this choice of stretching function, the thickest cells are distributed towards the bottom of the water column, offering the highest resolution towards the sea surface. This produces layers with mean thickness of 1.3 m (with minimum thickness of 0.7 m and maximum thickness of 2.2 m) over the continental shelf region shallower than 100 m, while along continental shelf in water between 100 m to 1000 m deep, the mean layer

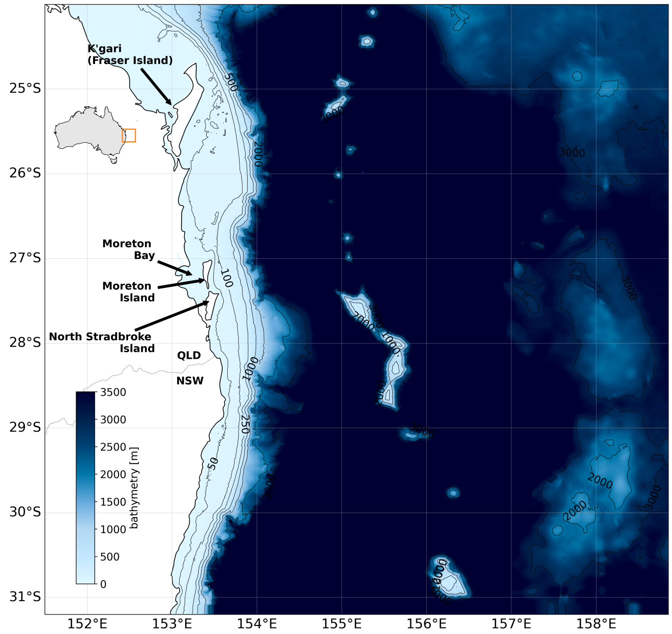

Figure 1. Model bathymetry map showing key features, including K'gari (Fraser Island), Moreton Island, North Stradbroke Island and Moreton Bay. The Queensland (QLD) and New South Wales (NSW) border (dotted line). Inset map shows Australia and model domain.

thickness is 9.4 m in the top 200 m and 17 m over the full column (with a minimum thickness of 1.7 m). For ocean cells deeper than 1000 m, the mean thickness is 100 m, with a minimum of 3 m. The model domain extends from $24°\mathrm{S}$ to $31.2°\mathrm{S}$ and from the coastline to $\sim 159°\mathrm{E}$, on a curvilinear Arakawa-C grid with horizontal resolution of approximately 900 m (with 733 by 718 tracer points). With a first baroclinic Rossby radius of deformation of $\sim 40-50\ \mathrm{km}$ (Chelton et al., 1998) in the South East Queensland region, this resolution will resolve a significant proportion of the submesoscale, as well as the mesoscale. The bathymetry is derived from the General Bathymetric Chart of the Oceans 2023 release (GEBCO Compilation Group, 2023), which is principally sourced from shipborne surveys over the continental shelf, and from a combined satellite-ship product in the deeper ocean. Bathymetry is smoothed to achieve a maximum $rx_0 = 0.33$, ensuring model stability while maintaining bedrock realism. We use the Generic Length Scale vertical mixing scheme (Umlauf and Burchard, 2003), which has also been shown to produce the largest magnitude of submesoscale kinetic and potential energy (Wang et al., 2022). Horizontal viscosity and diffusivity are set to minimal values (0.01 m^2/s) to reduce any artificial numerical damping.

Key features in the model domain are the coastline of South East Queensland and Northern New South Wales and the continental shelf break (Figure 1). Several large sand islands (K'gari, Moreton Island and North Stradbroke island) form a barrier on the relatively shallow continental shelf forming a large embayment (Moreton Bay) offshore of Brisbane. Several guyots (eroded and subsided volcanic seamounts), which top out at a bathymetry of $\sim$450 m, form a chain in the deep ocean, extending from the north to the south of the domain at $\sim 155.5°\mathrm{E}$. Within the domain, a total of $\sim$20 submarine canyons incise the continental shelf break (Huang et al., 2014).

The model surface and lateral boundaries are forced with reanalysis products through the period of simulation. The lateral boundaries are forced with temperature, salinity, free-surface variation and currents, obtained from the BlueLink ocean ReAnalysis (BRAN; Chamberlain et al., 2021). BRAN was chosen as the lateral boundary forcing product as it provides dynamically consistent, data-assimilative, mesoscale eddy-permitting ocean fields for the Australian region, ensuring accurate large-scale circulation and water mass properties at the model boundaries. Lateral boundaries are forced with the Flather scheme for 2D velocities, Radiation scheme for the free-surface, and the Radiation-Nudging scheme for 3D velocities and tracers (Marchesiello et al., 2001). The surface boundary is forced with wind stress, evaporative balance (as a virtual salt flux) and heat flux, extracted from the BARRA-R2 reanalysis (Su et al., 2025). This product has high spatial and temporal resolution, allowing for mesoscale atmospheric processes (e.g. storm events) to be resolved, which is particularly important for realistic heat and salt fluxes over the shallow continental shelf. Forcing for lateral and surface boundaries are applied at each model timestep, with linear interpolation between (daily) forcing fields. Like the lateral boundary conditions, the model initial conditions are sourced from BRAN, with the temperature and salinity taken for the 01-January-2012, and mapped to the model geometry using linear interpolation.

The model simulation period is chosen to be the year 2012, which was selected for the availability of observational studies for comparison (Sloyan et al., 2024) as well as the availability of the high-quality reanalysis forcing products (e.g. Chamberlain et al., 2021). Model spin-up was a repeat-year forcing of the 2012 forcing conditions.

3 Model evaluation & results

3.1 Mean state evaluation

We evaluate the ability of this SEQld ROMS configuration to represent the dominant surface and subsurface characteristics of the EAC, through the shelf and deep ocean regions offshore South East Queensland and Northern NSW. We first characterise the surface oceanography represented in the model, focussing on the mesoscale and longer-term variability through annual mean sea surface height (SSH), mean kinetic energy (MKE) and sea surface temperature (SST) maps (Figure 2).

Surface ocean characteristics are compared between observations and model output. The annual mean sea level from satellite-observed altimetry (IMOS, 2025b) shows close agreement (Figure 2a) with model free-surface elevation (Figure 2b), including the lower surface height over the continental shelf, higher SSH over most of the deep ocean, except for a persistent low SSH anomaly between $156°\mathrm{E}, 26-27°\mathrm{S}$ and in the far south of the domain at $158°\mathrm{E}, 31°\mathrm{S}$. For the 2012 year analysed here, the surface mean kinetic energy (calculated as $\mathrm{MKE} = \frac{1}{2}\left(\overline{u}^2 + \overline{v}^2\right)$, where u and v are the eastward and northward velocity components) is strongest along the continental shelf break, and weak through most of the rest of the domain, though there is some elevated energy in the clockwise circulation that concidies with the previously mentioned low SSH anomaly at $156°\mathrm{E}, 26-27°\mathrm{S}$ (Figure 2c). The model representation of the surface MKE field has the same broad pattern, though is distinctly weaker in the jet between $27°\mathrm{S}$ and $30°\mathrm{S}$ compared to the observations, noting that the observations are also inferred from a lower resolution satellite product and rely on an assumption of geostrophy. The distribution of recirculation features east of the EAC jet agree well with observations. The annual mean SST field (IMOS, 2025c), derived from satellite sensor

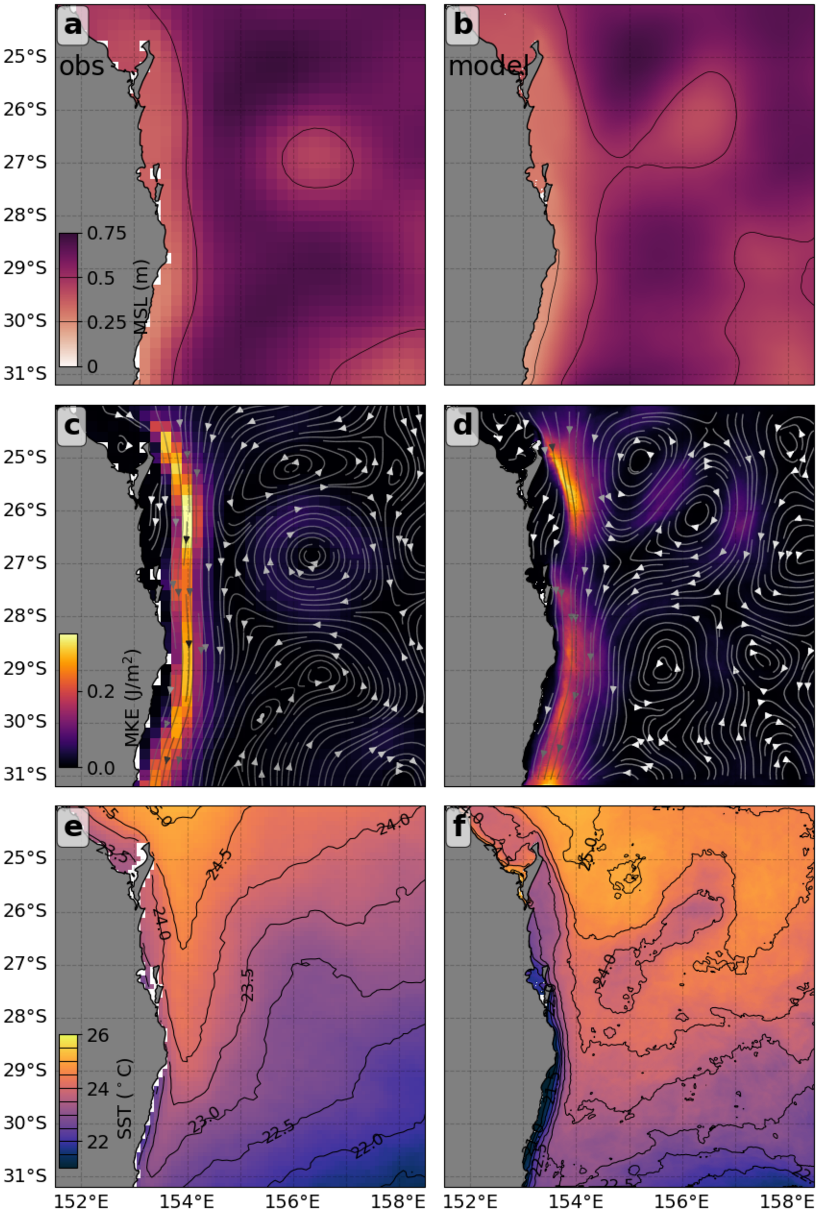

Figure 2. Surface ocean characteristics are compared between observations and model output. The annual mean sea level from (a) satellite-observed altimetry (IMOS, 2025b) and (b) model free-surface elevation SSH is compared. The annual mean surface kinetic energy field, with vectors streamline of mean surface velocity is shown from (c) satellite observations and (d) the model. In (c), satellite SSH observations are used to infer geostrophic velocities, from which the MKE and the streamlines are calculated. Surface temperature fields are compared between (e) satellite observations and (f) the model.

https://doi.org/10.5194/egusphere-2026-1852
Preprint. Discussion started: 18 May 2026

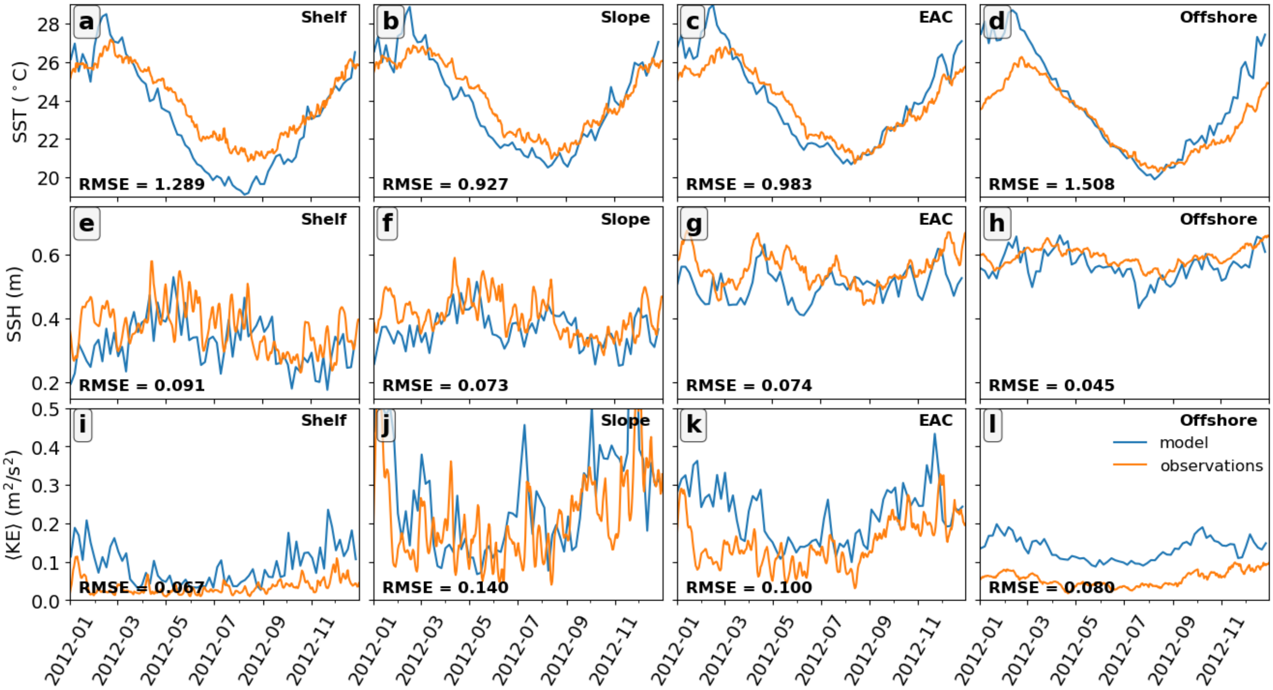

Figure 3. Timeseries of model (blue) and observations (orange) for (a-d) SST, (e-h) SSH and (i-l) spatial mean instantaneous kinetic energy ($\langle \mathrm{KE} \rangle$). In all panels, the root-mean-square error value ($\mathrm{RMSE} = \sqrt{(x_{\mathrm{model}}(t) - x_{\mathrm{obs}}(t))^2}$) is shown. The timeseries are calculated over four regions: the shelf (< 100 m deep), the slope (between 100 m to 1500 m deep, and west of 154.3°E), the EAC region (deeper than 90 m and west of 155°E, and offshore (east of 155°E).

product (RAMSSA; Beggs et al., 2011), displays a pattern of generally cooling temperatures with increasing latitude, with a tongue of warmer surface water close to the coast carried by the EAC jet (Figure 2e). The model representation of this field is good, with a broad pattern of decreasing temperature with increasing latitude, though the eastern half of the domain displays a warm bias.

Timeseries of spatially-averaged SST (Figure 3a-d), SSH (Figure 3e-h) and kinetic energy (Figure 3i-l) are compared between the model (blue line) and observations (orange line). This analysis is further broken up, with spatial averages over four regions: shelf, slope, EAC and offshore (with region definitions given in the caption). The root-mean-square error ($\mathrm{RMSE} = \sqrt{(x_{\mathrm{model}}(t) - x_{\mathrm{obs}}(t))^2}$) between model and observation is shown for each series. There is generally good agreement between model and observation. The model representation of SST is slightly high in summer, though very reasonable through the rest of the year. Likewise, SSH is represented with low RMSE through the year, especially given that the exact details of the mesoscale circulation (and hence SSH) would not be expected to be represented with the correct timing without any data assimilation (Figure 3e-f). Kinetic energy is shown to be stronger in the model, but this represents the extra energy captured in the submesoscale permitting simulation, compared to the coarse resolution satellite altimery that produces the geostrophic

https://doi.org/10.5194/egusphere-2026-1852
Preprint. Discussion started: 18 May 2026

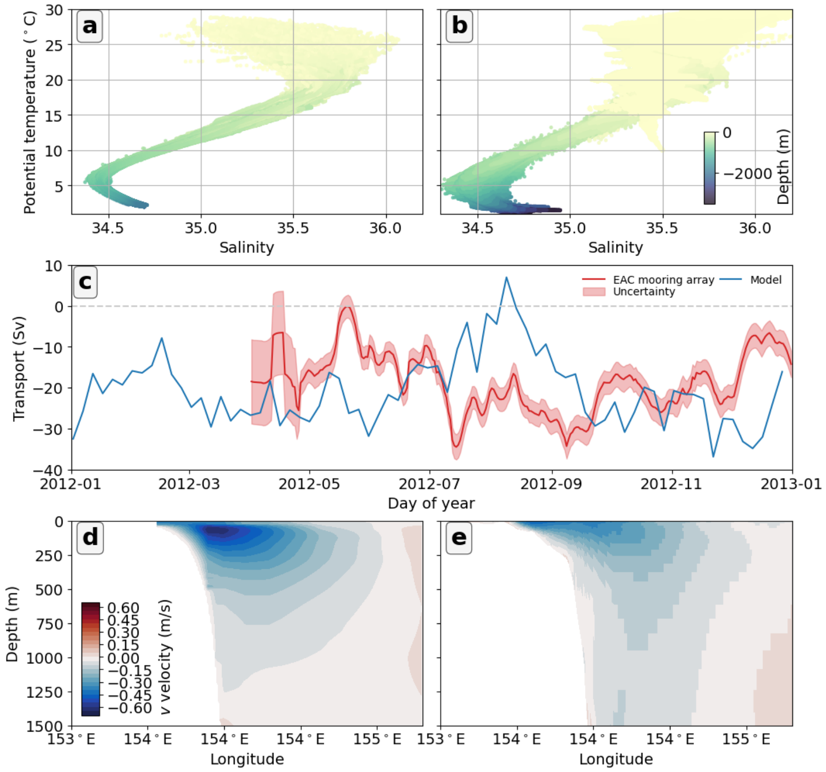

Figure 4. θ-S diagrams of water properties throughout 2012 are compared between (a) profiling Argo float measurements and (b) ocean model conditions. The 2012 net volume transport through the ∼27°S latitude is compared for observations from the (c) EAC mooring array (red) and the ocean model (blue). The annual mean state meridional (v) velocity from (d) the EAC moorings and (e) model is compared. In (b), only wintertime and summertime snapshots are combined to reduce data density. In (c), the data uncertainty is shaded.

velocities required for calculating the kinetic energy (e.g. Figure 3k-l). Shelf observations may also contain significant error - arising from coarse resolution and complex coastal geography - such that the model representation may in fact be closer to reality than implied by the calculated RMSE (e.g. Figure 3a). Overall, the RMSE values show good agreement with the observed temporal evolution - this complements the realistic spatial representation shown above.

An accurate subsurface representation is important for capturing density gradients that set pressure gradients and for water-mass properties, as well as understanding baroclinic instability. Profiling float observations (IMOS, 2025a) taken from Argo floats (Wong et al., 2020) throughout the model domain region, display a typical subtropical ocean θ-S relationship (Figure 4a). These water masses comprise warm, saline surface waters that transition to a salinity minimum at depth, before retroflecting to a higher salinity, temperature minimum at the bottom. This represents the warm and saline subtropical surface waters advected southwards by the EAC, overlying Sub-Antarctic Mode Water, Antarctic Intermediate Water at the salinity minimum (Bostock et al., 2013), and Lower Circumpolar Deep Water at the bottom (Sokolov and Rintoul, 2000). This distribution is well represented in the model (Figure 4b), though it displays larger variation - likely due to the large region captured by the model

https://doi.org/10.5194/egusphere-2026-1852
Preprint. Discussion started: 18 May 2026

compared to the biased locations sampled by Argo. The total transport through ∼27°S, as captured by the EAC mooring array (Figure 4c), varies between 5 Sv northward to 35 Sv southward with periods of stronger and weaker transport. The model similarly shows variability between 5 Sv northward to 35 Sv southward. The model EAC transport has a similar seasonal cycle, but appears to be slightly delayed, with the observed period of northward flow in May, being delayed in the model until September. Annual-mean meridional v-velocity transects measured by the EAC mooring array (Figure 4d) compared to velocity in the model at the same latitude (Figure 4e) display differences in the magnitude of velocity close to the surface (above 250 m), with the model velocities being too weak. Below this depth, the velocity structure is remarkably similar between observation and model, with the strong southwards flowing jet and deep extension of the current.

Overall, the model represents the mesoscale and mean circulation relatively realistically, with good representation of the SSH field and the broader patterns in MKE and SST. The subsurface oceanography is particularly well represented, with representative temperature and salinity properties and transport through the EAC. The biases (low EAC jet MKE through the south of the domain and warm SST over the east of the domain) are not considered to be fundamental issues. This is because the MKE varies through the year, with the periods of high and low energy, and hence transport, which are well captured by the model (as shown in Figure 4c,d). Furthermore, the purpose of this model was developed to exploit the high spatial resolution to examine submesoscale processes, for which these biases are not critical. Assimilation of SST and SSH fields would dramatically improve the mesoscale circulation (e.g. Gwyther et al., 2022), but at the the cost of degrading subsurface baroclinic modes and energy pathways - features that are important to preserve for a physically realistic representation of submesoscale dynamics.

4 Submesoscale dynamics

To demonstrate the emergence of submesoscale features in this model, Rossby number, horizontal divergence and density gradient are analysed at three time slices (Figure 5). The relative vorticity normalised by the Coriolis parameter represents the relative contribution of local rotation compared to planetary rotation, i.e. the Rossby number; $\mathrm{Ro} \sim \frac{\zeta}{f}$, where ζ is the relative vorticity defined as $\zeta = \frac{\partial v}{\partial x} - \frac{\partial u}{\partial y}$ and f is the Coriolis parameter. The magnitude of the Rossby number indicates whether the flow is geostrophic ($|\mathrm{Ro}| \ll 1$), mostly geostrophic - but with important ageostrophic corrections ($|\mathrm{Ro}| \sim 1$), or where geostrophy has broken down ($|\mathrm{Ro}| \gtrsim 1$) due to the dominance of submesoscale processes. The horizontal flow divergence, $\delta = \nabla_h \cdot \mathbf{u} = \frac{\partial u}{\partial x} + \frac{\partial v}{\partial y}$, indicates lateral expansion or contraction of fluid parcels, and when normalised by f, values of $\frac{\delta}{f} \sim \mathcal{O}(1)$ indicate submesoscale activity often associated with frontal and filamentary flow. This metric complements the Rossby number by directly identifying areas of pronounced ageostrophic motion which can contribute to vertical exchange. The horizontal density gradient $|\nabla_h \rho| = \sqrt{\frac{\partial \rho}{\partial x}^2 + \frac{\partial \rho}{\partial y}^2}$, where ρ is the seawater density, quantifies lateral variations in seawater density. Regions of strong density gradient indicate sharp spatial contrasts in temperature and/or salinity – these gradients can store potential energy that can be subsequently released through instabilities that drive ageostrophic circulation. While this is not a specifically submesoscale quantity, co-alignment of sharp density gradients with high Rossby number, or horizontal divergence, indicates frontal activity that has been developed by submesoscale processes.

https://doi.org/10.5194/egusphere-2026-1852
Preprint. Discussion started: 18 May 2026

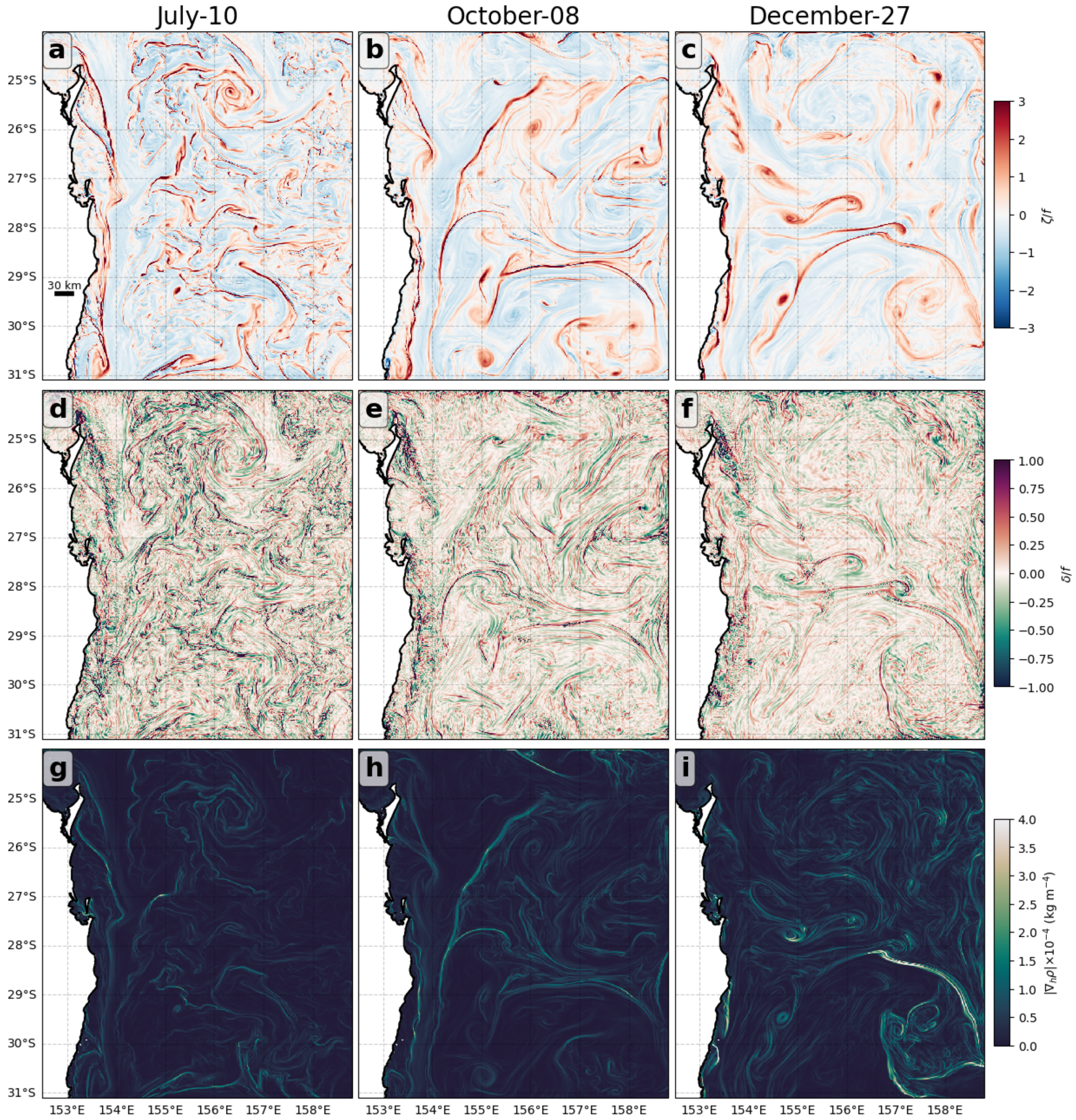

Figure 5. Diagnostics of submesoscale activity are presented, showing (a-c) the normalised relative vorticity (i.e. Rossby number), (d-e) the horizontal convergence, and (g-i) the horizontal density gradient $|\nabla_h \rho|$. These fields are calculated for several snapshot periods, (a,d,g) 10-July, (b,e,h) 08-October and (c,f,i) 27-December. These periods were chosen to highlight times with strong submesoscale activity across both winter and summer. In (a), a length scale marker indicates the approximate boundary between mesoscale and submesoscale motions at this latitude.

Rossby number at the three time slices show widespread occurrences of $|\mathrm{Ro}| > 1$: along the inland edge of the EAC jet (Figure 5a), along elongated filaments (e.g. Figure 5b) and in small submesoscale eddies (e.g. Figure 5c). Likewise, the divergence fields have patches of $\mathcal{O}(1)$ which shift through time, as well as regions of consistent $\mathcal{O}(1)$, for example, downstream of K'gari (Figure 5e-f). Filaments of strong horizontal density gradient emerge throughout the domain at each snapshot (Figure 5g-i) and are generally co-located with strong Rossby number. The signature of the EAC is visible at each time through the bands of elevated vorticity, divergence or density gradient on the edges of this jet.

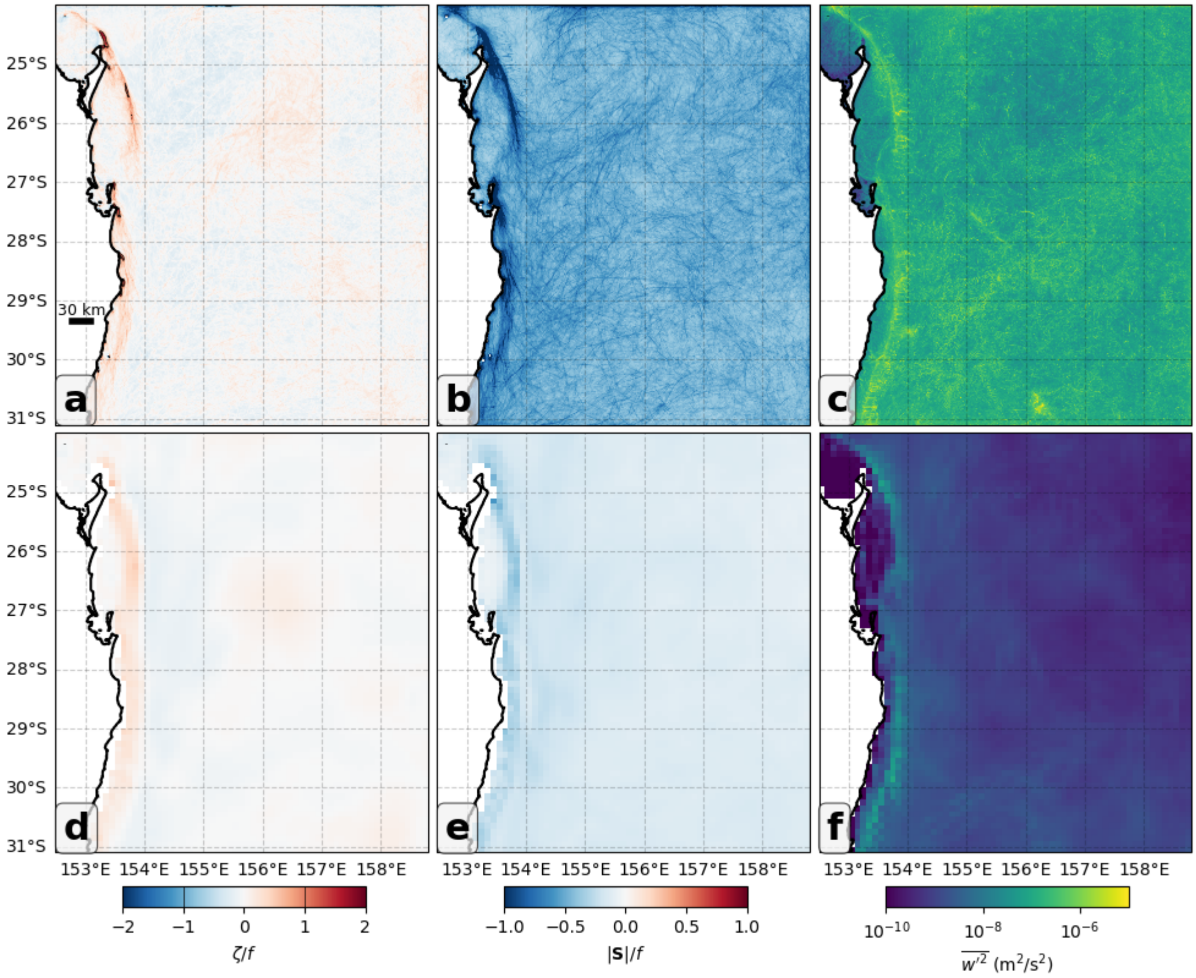

Figure 6. Time-mean diagnostics from (a-c) this ocean model are compared to (d-f) BRAN. The annual-mean Rossby number (ζ/f) for our model (a) and (d) BRAN are compared. The normalised magnitude of strain ($|\mathbf{S}|/f$) is shown for (b) our model and (e) BRAN. The vertical velocity variance ($\overline{w'^2}$), averaged over the top 100 m, is shown for (c) our model and (f) BRAN. In (c,f) the colour axis is logarithmic.

We present a comparison between our model (Figure 6a-c) and BRAN (Figure 6d-f) to illustrate the difference between our submesoscale permitting model and a commonly-used mesoscale permitting model, BRAN. As BRAN assimilates a broad

https://doi.org/10.5194/egusphere-2026-1852
Preprint. Discussion started: 18 May 2026

range of observational products, it produces a surface representation of the mesoscale ocean with low error. It would be unfair to expect time slices from this SEQld ROMS model and BRAN to be closely aligned, especially for rapidly evolving submesoscale metrics, and so we compare annual-mean fields of Rossby number (ζ/f), magnitude of the total strain, normalised by the Coriolis parameter ($|\mathbf{S}|/f$) and the variance in the vertical velocity ($\overline{w'^2}$), averaged over the top 100 m. The Rossby number shows broadly similar patterns between SEQld ROMS and BRAN, with higher Rossby number over the continental shelf (Figure 6a,d). The hotspots of persistent elevated Rossby number emerge in the wake of the coastal islands and headland promontories, which are resolved only in SEQld ROMS. The horizontal velocity gradient may be decomposed into divergent, rotational and strain components. The strain component is characterised by normal and shear components that represent deformation of the flow through stretching and compression with constant area. The magnitude of strain, $|\mathbf{S}| = \sqrt{\left(\frac{\partial u}{\partial x} - \frac{\partial v}{\partial y}\right)^2 + \left(\frac{\partial u}{\partial y} + \frac{\partial v}{\partial x}\right)^2}$, captures the combined stretching and compression associated with this deformation and acts to sharpen lateral temperature and salinity gradients, thus generating and maintaining fronts and submesoscale features. The ROMS simulation (Figure 6b) displays significantly stronger strain along the EAC jet in the wake of the coastal islands, as well as across the domain as a whole, as compared to BRAN (Figure 6e). The variance in vertical velocity is defined as $\overline{w'^2} = \overline{(w - \overline{w})^2}$, where the w is the vertical velocity field and an overline, $\overline{(\cdot)}$ denotes the time-mean operator. Vertical velocity is diagnosed from the continuity equation under the hydrostatic approximation in both of these models. While non-hydrostatic vertical accelerations are neglected, the vertical velocity variance represents the resolved horizontal divergence and associated ageostrophic vertical circulation. The vertical velocity variance is at least an order of magnitude higher in the higher resolution ROMS simulation as compared to BRAN (Figure 6c,f). These metrics indicate stronger rotational ageostrophy, enhanced strain associated with frontogenesis, and larger vertical velocity variability in the ROMS simulations. This reflects the ability of the higher-resolution ROMS configuration to resolve submesoscale and partially unbalanced motions, that are parameterised or smoothed in coarser simulations (such as BRAN).

To calculate the kinetic energy spectra (Figure 7a), two-dimensional Fourier transforms are applied to the horizontal velocity components u and v. Spectral kinetic energy density is then computed using Parseval's theorem as $E(k_x, k_y) = \frac{1}{2}(|\hat{u}|^2 + |\hat{v}|^2)$ where $\hat{u}$ and $\hat{v}$ are the Fourier components. The resulting two-dimensional spectrum is converted to a one-dimensional isotropic spectrum by computing the total wavenumber magnitude $k = \sqrt{k_x^2 + k_y^2}$ and radially binning energy into annuli of constant k. This produces the isotropic kinetic energy spectrum $E(k)$, which represents the distribution of kinetic energy across spatial scales. Motions at length scale λ correspond to wavenumber $k = 1/\lambda$. The reference slopes k^{-3} and $k^{-5/3}$ indicates power law behaviour of the kinetic energy spectrum, where the slope describes how kinetic energy is distributed across spatial scales (Callies, 2019). A spectrum approaching $\sim k^{-3}$ is consistent with quasi-geostrophic dynamics, in which velocity varies smoothly in space and most kinetic energy resides in the mesoscale (Charney, 1971). A shallower spectrum closer to $k^{-5/3}$ indicates a larger contribution from ageostrophic or submesoscale motions, which introduce sharper fronts and smaller-scale variability and therefore increase the relative energy at high wavenumbers (Rocha et al., 2016). Slopes steeper than k^{-3} (e.g. $\sim k^{-4}$) may imply rapid removal of small-scale variance due to dissipation, or limited observational resolution. The effective model resolution, defined as the spatial scale at which the model kinetic energy departs from the nominal regime, is typically

https://doi.org/10.5194/egusphere-2026-1852
Preprint. Discussion started: 18 May 2026

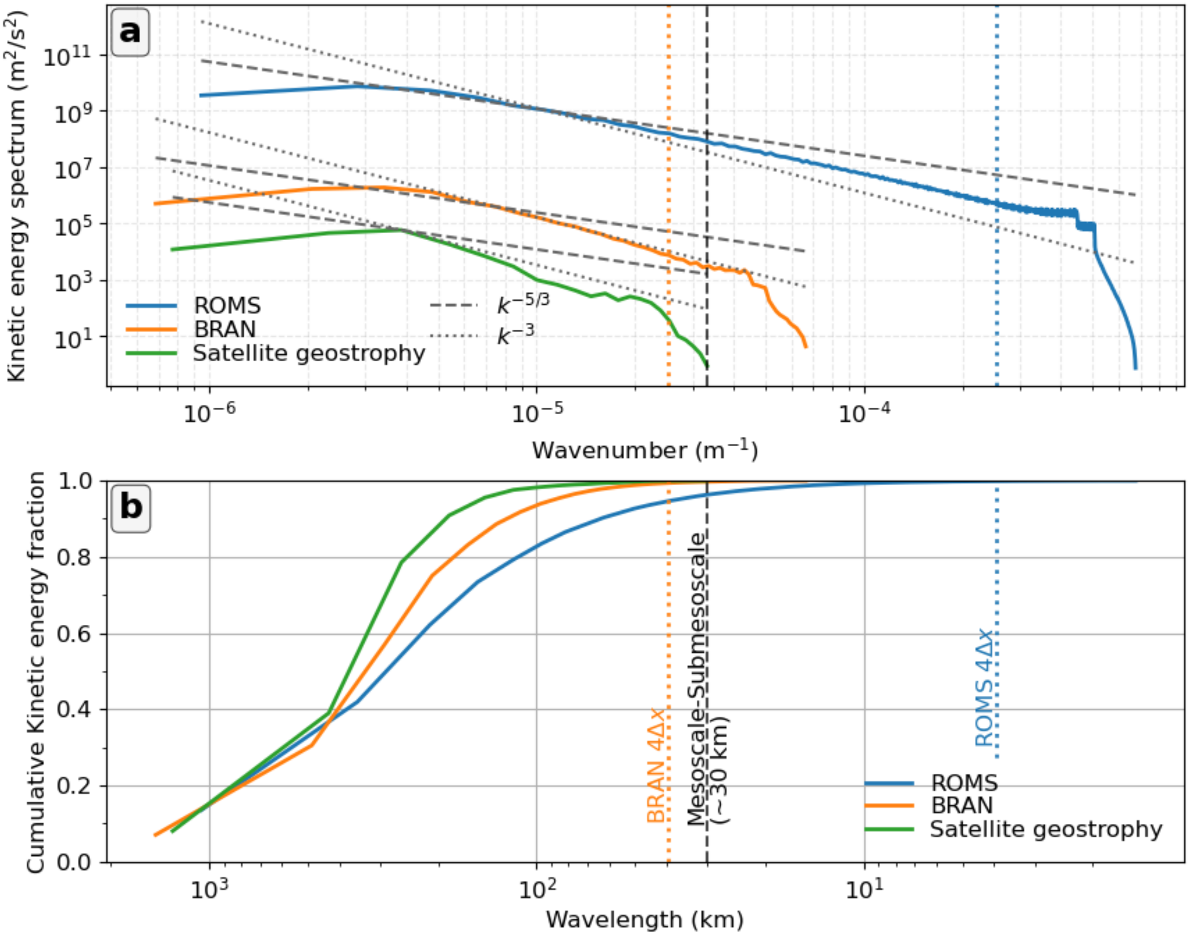

Figure 7. (a) The spectrum of the spatial kinetic energy distribution against wavenumber, $E(k)$, computed from surface velocities is shown for ROMS (blue line), BRAN (orange line), and geostrophic currents sourced from satellite altimetry (green line). Spectra is shown as a function of horizontal wavenumber k, with dashed and dotted lines showing reference slopes $k^{-5/3}$ and k^{-3}, while vertical lines show the effective model resolution $(4\Delta x)$ for ROMS (blue line) and BRAN (orange line), and an indicative mesoscale-submesoscale boundary at $30\ \mathrm{km}$. (b) The corresponding cumulative fraction of the total kinetic energy is shown as a function of wavelength, for ROMS (blue line), BRAN (orange line) and geostrophic currents (green line).

larger than the horizontal grid spacing (Soufflet et al., 2016). Here we use a value of $4\Delta x$ to show an approximate scale below which model numerical dissipation influences dynamics.

ROMS exhibits a larger KE magnitude across scale, compared to the coarser-resolution BRAN, and even larger compared to satellite-derived geostrophic KE (Figure 7a). The spectral slopes show that ROMS has the shallowest gradient, closest to $k^{-5/3}$, indicating significant submesoscale activity. BRAN closely follows the k^{-3} relationship, consistent with quasi-geostrophic dynamics, but with limited submesoscale energy, and the satellite geostrophy has a steeper slope than k^{-3} indicating likely

https://doi.org/10.5194/egusphere-2026-1852
Preprint. Discussion started: 18 May 2026

damping and observational smoothing. Furthermore, ROMS carries energy into the submesoscale (beyond the 30 km boundary), while spectra of BRAN and satellite observations either capture the transition or roll off before this transition. The roll off in model KE near the effective resolution is expected. Together, this shows that at the large scale, the spectral energy distribution of all systems is comparable, but below $\sim 100\ \mathrm{km}$, the submesoscale processes, permitted with the resolution used in this SEQld ROMS application, are an important contributor to energy dynamics.

The cumulative fraction of the total for each spectra shows that the total KE in the domain is reached at larger spatial scales for the satellite-derived and BRAN, compared to ROMS (Figure 7b). The ROMS simulation derives $\sim 4\%$ of the total KE from processes occurring in the submesoscale, as opposed to BRAN (0.3%). Together, Figure 7 illustrates the richer, more energetic spectrum of dynamics that emerges from the higher resolution ROMS simulation.

An example assessment of submesoscale processes is conducted for the continental shelf in the vicinity of K'gari (Figure 8). This region exhibits strong emergence of submesoscale activity even under an annual-mean, indicating submesoscale features that are persistent throughout the year. The surface ocean displays elevated small-scale rotation (Rossby number) and local patches of divergence and convergence (Figure 8a,b), as well as a band of strong strain (Figure 8c), all of which initiate upstream of K'gari, propagate past the island, and extend downstream shorewards of the 100 m bathymetric contour, before dying out as the bathymetry sweeps inland at $\sim$26.5°S. The surface horizontal density gradient over the shelf and downstream of island promontories displays elevated values (Figure 8d), indicating the sharpening of density gradients relative to the more weakly stratified open ocean. This pattern is consistent with wake-driven strain and shear downstream of K'gari, together with flow-bathymetry interactions along the continental shelf edge, which act to intensify density fronts and generate persistent submesoscale frontal hotspots. A vertical transect at 25°S (see Figure 8a for location) shows strong subsurface vertical velocity variance and elevated values over the continental slope (Figure 8e). Along the same transect, the isopycnal slope ($s = \frac{|\nabla_h \rho|}{|\partial\rho/\partial z|}$) shows steepened isopycnals over the shallow waters ($< 100\ \mathrm{m}$ deep) immediately seaward of K'gari, as well as on the continental slope at 153.75°E (Figure 8f).

These diagnostics illustrate that the continental shelf region to the north and east of K'gari is a region of intense submesoscale activity that is persistent over long timescales, rather than being stochastic events. The enhanced Ro, δ and $|\mathbf{S}|$ are evident upstream of the northern tip of K'gari and extend downstream along the shelf edge, largely confined landward of the 100 m isobath. This spatial distribution suggests that submesoscale activity is closely associated with the East Australian Current impinging on the continental shelf, combined with local enhancement by the coastal promontory along the eastern boundary of K'gari. The vertical transects display relatively high vertical velocity variance and increased isopycnal slope over the continental shelf, as well as even higher rates on the continental slope. These factors thus suggest that submesoscale activity, shown through elevated vorticity, strain and divergence, is associated with increased vertical motion particularly in the subsurface, as well as steepening of isopycnals typically associated with frontogenesis. The persistent submesoscale activity north and east of K'gari likely contributes to the upstream adjustment region of the EAC intensification zone. In particular, the elevated strain and vorticity resolved by the model demonstrates active frontogenesis at the shelf edge. Frontal sharpening converts available potential energy into kinetic energy, accelerating the flow, while the accompanying divergence indicates

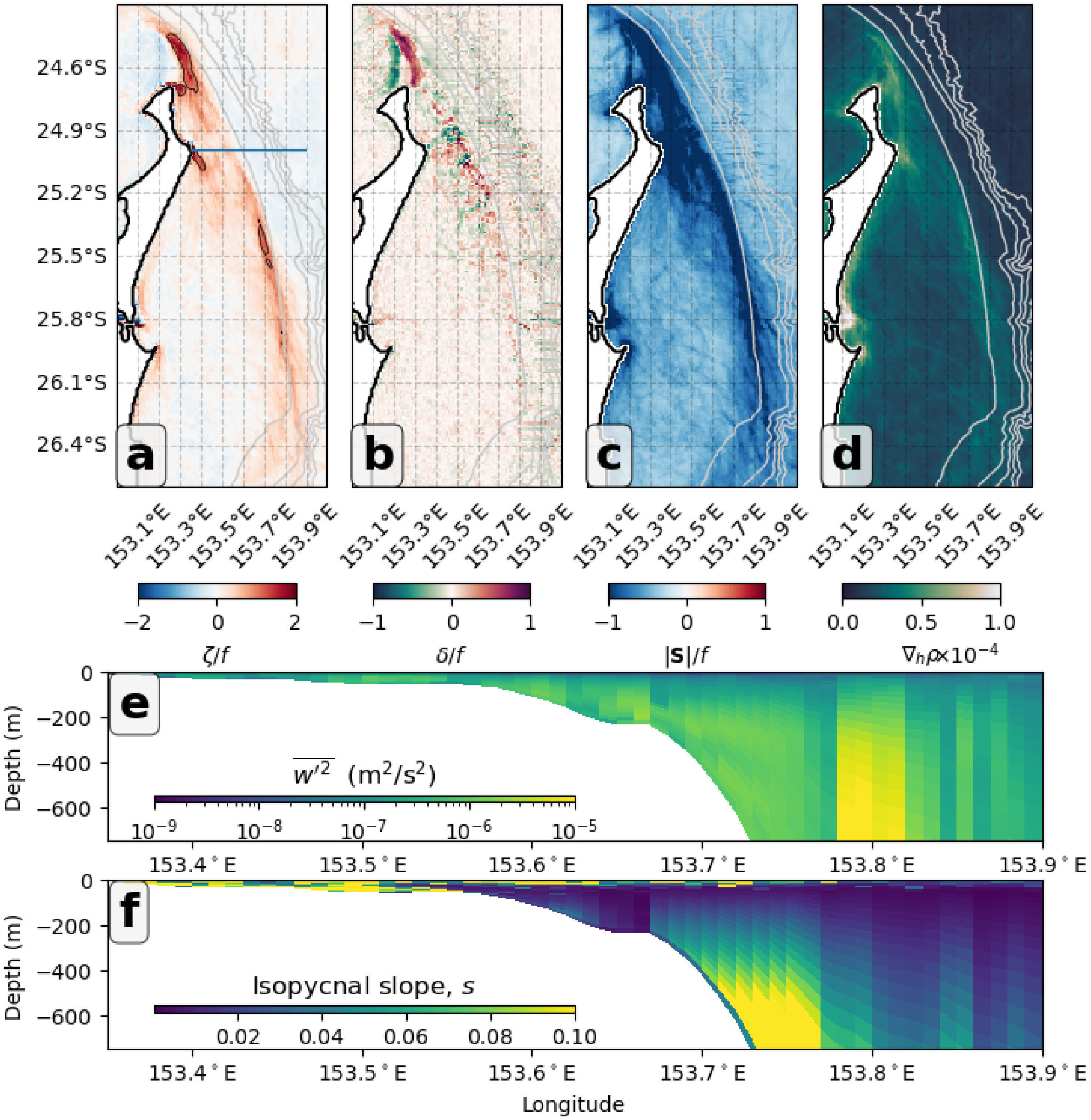

Figure 8. Annual-mean (a) Rossby number ζ/f, (b) normalised horizontal divergence δ/f, (c) normalised magnitude of strain $|\mathbf{S}|/f$ (d) horizontal density gradient $\nabla_h \rho$ are shown for the region east of K'gari. Black contour in (a) is for $|\mathrm{Ro}| = 1$. Vertical profiles of (e) vertical velocity variance and (f) isopycnal slope ($s = \frac{|\nabla_h \rho|}{|\partial \rho/\partial z|}$) are shown for the transect illustrated by the blue line in (a).

lateral contraction of the jet, which further enhances acceleration. In addition, headland-generated vorticity along the coastline modifies the local flow structure and may contribute to instability development downstream near the separation zone.

https://doi.org/10.5194/egusphere-2026-1852
Preprint. Discussion started: 18 May 2026

5 Discussion

We have developed a model application that has been specifically chosen to focus on the EAC intensification zone with a horizontal resolution chosen to allow the development of submesoscale dynamics. The South East Queensland and Northern New South Wales continental shelf represents an under researched corner between the more heavily researched regions of the Great Barrier Reef (e.g. Baird et al., 2021; Steven et al., 2019) and the separation zone of the East Australian Current further south (e.g. Kerry and Roughan, 2020). Additionally, larger-scale models which represent this study area, such as BRAN, provide time-accurate representations of the mesoscale circulation, which are well suited to studies of mesoscale variability and boundary current dynamics, but necessarily under-represent submesoscale processes due to their coarser resolution. The present model therefore represents an important step towards resolving the multiscale dynamics of the East Australian Current system in the intensification zone, enabling process-based investigation of how mesoscale and submesoscale processes interact along the continental shelf in this region.

The results of this study demonstrate that the SEQld ROMS presented here produces a dynamically rich submesoscale field, in addition to a realistic representation of the mesoscale circulation. The simulated submesoscale activity, characterised by enhanced stretching, rotation and horizontal divergence, manifests as sharp fronts, filaments and small eddies occurring at spatial scales finer than those resolved in many existing model configurations of the region. These features are associated with increased horizontal and vertical velocities and elevated variability in these fields. Such variability is consistent with enhanced vertical and lateral exchange processes, which are known to influence nutrient distribution, upwelling, and cross-shelf exchange (Klein et al., 2008; Balwada et al., 2018).

The submesoscale characteristics exhibited by the model are consistent with a growing body of observational and modelling studies documenting energetic submesoscale activity along the inshore edge of the EAC. Observations from HF radar and in situ measurements have identified high Rossby number filaments (Mantovanelli et al., 2017), vertical shear (Archer et al., 2020) strong frontal strain and regions of enhanced convergence and divergence (Schaeffer et al., 2017). These studies further emphasise the inshore edge of the EAC as a hotspot for vorticity generation (Kerry et al., 2020), with the shelf-boundary current interaction as a key trigger (e.g. Mantovanelli et al., 2017). In this context, the emergence of elevated vorticity upstream of K'gari in the present model, and the subsequent propagation of these anomalies along the continental shelf break, is consistent with boundary current impingement and shelf-current interactions. Modelling studies of other shelf-boundary current systems have suggested that submesoscale frontogenesis at prominent headlands is a result of coastline influenced vorticity generation, which is then amplified by horizontal advection (e.g. Dauhajre et al., 2017).

The KE spectra indicate that while comparable to coarser-resolution models at mesoscale wavelengths, ROMS retains substantially more energy at smaller scales and exhibits a shallower spectral slope, consistent with enhanced ageostrophic and submesoscale motions enabled by its finer grid spacing. The cumulative spectra confirm that submesoscale processes contribute a meaningful fraction of total kinetic energy in ROMS but are largely absent in the coarser systems.

The purpose of this model is to resolve the mesoscale circulation of the EAC intensification zone and the submesoscale variability associated with fronts, filaments and boundary current-shelf interactions. Thus, it is suited for process studies of shelf-boundary current dynamics, and particularly for the diagnosis of mechanisms driving and resulting from submesoscale activity. It can also be used as a physical backbone for ecosystem and biogeochemistry models, sediment transport and resuspension studies and larval dispersal experiments. The submesoscale-resolving dynamics are particularly relevant for nutrient injection into the euphotic zone and cross-shelf exchange pathways. We anticipate that the mechanistic understanding developed from this model will also apply more broadly to other shelf systems and western boundary currents.

However, some processes are not resolved or parameterised in the model, in particular tides and river sources. The absence of barotropic and baroclinic tides may impact representation of shelf/slope mixing and energy dissipation, while the lack of river discharge and associated buoyancy input will affect coastal stratification. The chosen boundary conditions (BRAN) and surface forcing products (BARRA) adequately capture mesoscale circulation and surface heat and salt fluxes, as well as daily forcing wind, though sub-daily variability may be under-represented. We argue that these are acceptable due to the initial design focus: resolving submesoscale processes over the continental shelf and slope, and their interactions with the mesoscale circulation. As this model is not data assimilating, it is not designed for predictive skill of individual events. Phase errors in mesoscale features should be expected and submesoscale features should be interpreted statistically and mechanistically, not as exact realisations. Nevertheless, the absence of assimilation avoids the unphysical adjustment of vertical modes leading to degradation of subsurface representation (e.g. Gwyther et al., 2023a, b). This model complements existing forecast studies (e.g. Kerry et al., 2026) by providing a dynamically rich, high-resolution framework for examining the processes driving the emergence of submesoscale dynamics.

Future development will include extension to longer, interannual simulations allowing examination of longer-term variability and large-scale climate forcing as well as incorporation of additional physical forcing, such as tides and river discharge, to improve shelf mixing and coastal stratification.

6 Conclusions

We have developed and assessed a high resolution, submesoscale-permitting ocean simulation of the intensification zone of the East Australian Current and adjacent shelf sea, in the South East Queensland and Northern New South Wales region of Eastern Australia. This model captures the mean mesoscale structure and variability of the EAC well, especially for a non-assimilative configuration. The fine horizontal resolution allows the emergence of submesoscale features such as eddies, fronts and filaments. This submesoscale activity arises naturally from the resolved dynamics, and preliminary analysis indicates the downstream wakes of the coastal islands as hotspots of persistent submesoscale activity. This model complements existing coarser reanalysis products, by resolving processes that are otherwise parameterised. We anticipate that this model will be useful for developing process-based understanding of this complex and energetic Western Boundary Current.

Code and data availability. The current version of ROMS is available from the ROMS website (www.myroms.org/) under the MIT/X license. The exact version of the model used to produce the results used in this paper is archived on repository at https://doi.org/10.5281/

zenodo.19247625 (Gwyther et al., 2026), as are input data and scripts to run the model. Code used to produce all figures presented in this paper are archived at https://doi.org/10.5281/zenodo.19230573 (Gwyther, 2026).

Author contributions. DEG designed and developed the model application with assistance from MJ. DEG performed the simulations. DEG prepared the manuscript with contributions from MJ and HB.

Competing interests. The authors declare that they have no conflict of interest.

Acknowledgements. Data was sourced from Australia's Integrated Marine Observing System (IMOS) – IMOS is enabled by the National Collaborative Research Infrastructure strategy (NCRIS).

https://doi.org/10.5194/egusphere-2026-1852
Preprint. Discussion started: 18 May 2026

References

Aijaz, S., Colberg, F., and Brassington, G. B.: Lagrangian and Eulerian Modelling of River Plumes in the Great Barrier Reef System, Australia, Ocean Modelling, 188, 102 310, https://doi.org/10.1016/j.ocemod.2023.102310, 2024.

Archer, M., Schaeffer, A., Keating, S., Roughan, M., Holmes, R., and Siegelman, L.: Observations of Submesoscale Variability and Frontal Subduction within the Mesoscale Eddy Field of the Tasman Sea, Journal of Physical Oceanography, 50, 1509–1529, https://doi.org/10.1175/JPO-D-19-0131.1, 2020.

Archer, M. R., Roughan, M., Keating, S. R., and Schaeffer, A.: On the Variability of the East Australian Current: Jet Structure, Meandering, and Influence on Shelf Circulation, Journal of Geophysical Research: Oceans, 122, 8464–8481, https://doi.org/10.1002/2017JC013097, 2017.

Azaneu, M. V. C., Roughan, M., Keating, S. R., Schaeffer, A., and Schallenberg, C.: Characterising Submesoscale Processes, Uplift and Subduction across Diverse Fronts in the East Australian Current System, Progress in Oceanography, p. 103690, https://doi.org/10.1016/j.pocean.2026.103690, 2026.

Baird, M. E. and Ridgway, K. R.: The Southward Transport of Sub-Mesoscale Lenses of Bass Strait Water in the Centre of Anti-Cyclonic Mesoscale Eddies, Geophysical Research Letters, 39, https://doi.org/10.1029/2011GL050643, 2012.

Baird, M. E., Mongin, M., Skerratt, J., Margvelashvili, N., Tickell, S., Steven, A. D. L., Robillot, C., Ellis, R., Waters, D., Kaniewska, P., and Brodie, J.: Impact of Catchment-Derived Nutrients and Sediments on Marine Water Quality on the Great Barrier Reef: An Application of the eReefs Marine Modelling System, Marine Pollution Bulletin, 167, 112 297, https://doi.org/10.1016/j.marpolbul.2021.112297, 2021.

Balwada, D., Smith, K. S., and Abernathey, R.: Submesoscale Vertical Velocities Enhance Tracer Subduction in an Idealized Antarctic Circumpolar Current, Geophysical Research Letters, 45, 9790–9802, https://doi.org/10.1029/2018GL079244, 2018.

Beggs, H. M., Zhong, A., Warren, G., Alves, O., Brassington, G. B., and Pugh, T.: RAMSSA - An Operational, High-Resolution, Regional Australian Multi-Sensor Sea Surface Temperature Analysis over the Australian Region, Australian Meteorological and Oceanographic Journal, 61, 1–22, 2011.

Bostock, H. C., Sutton, P. J., Williams, M. J. M., and Opdyke, B. N.: Reviewing the Circulation and Mixing of Antarctic Intermediate Water in the South Pacific Using Evidence from Geochemical Tracers and Argo Float Trajectories, Deep Sea Research Part I: Oceanographic Research Papers, 73, 84–98, https://doi.org/10.1016/j.dsr.2012.11.007, 2013.

Bourg, N., Schaeffer, A., and Molcard, A.: East Australian Current System: Frontal Barrier and Fine-Scale Control of Chlorophyll-a Distribution, Journal of Geophysical Research: Oceans, 129, e2023JC020 312, https://doi.org/10.1029/2023JC020312, 2024.

Callies, J.: Submesoscale Dynamics Inferred from Oleander Data, Oceanography, 33, 138–139, https://doi.org/10.5670/oceanog.2019.320, 2019.

Capet, X., McWilliams, J., Molemaker, M., and Shchepetkin, A.: Mesoscale to Submesoscale Transition in the California Current System. Part II: Frontal Processes, Journal of Physical Oceanography, 38, 44–64, https://doi.org/10.1175/2007JPO3672.1, 2008.

Cetina-Heredia, P., Roughan, M., van Sebille, E., and Coleman, M. A.: Long-Term Trends in the East Australian Current Separation Latitude and Eddy Driven Transport, Journal of Geophysical Research: Oceans, 119, 4351–4366, https://doi.org/10.1002/2014JC010071, 2014.

Chamberlain, M. A., Oke, P. R., Fiedler, R. A. S., Beggs, H. M., Brassington, G. B., and Divakaran, P.: Next Generation of Bluelink Ocean Reanalysis with Multiscale Data Assimilation: BRAN2020, Earth System Science Data, 13, 5663–5688, https://doi.org/10.5194/essd-13-5663-2021, 2021.

Chapman, C. C., Sloyan, B. M., Schaeffer, A., Suthers, I. M., and Pitt, K. A.: Offshore Plankton Blooms via Mesoscale and Sub-Mesoscale Interactions With a Western Boundary Current, Journal of Geophysical Research: Oceans, 129, e2023JC020 547, https://doi.org/10.1029/2023JC020547, 2024.

Charney, J. G.: Geostrophic Turbulence, Journal of the Atmospheric Sciences, 28, 1087–1095, https://doi.org/10.1175/1520-0469(1971)028<1087:GT>2.0.CO;2, 1971.

Chelton, D. B., deSzoeke, R. A., Schlax, M. G., Naggar, K. E., and Siwertz, N.: Geographical Variability of the First Baroclinic Rossby Radius of Deformation, Journal of Physical Oceanography, 28, 433–460, https://doi.org/10.1175/1520-0485(1998)028<0433:GVOTFB>2.0.CO;2, 1998.

Dauhajre, D. P., McWilliams, J. C., and Uchiyama, Y.: Submesoscale Coherent Structures on the Continental Shelf, Journal of Physical Oceanography, 47, 2949–2976, https://doi.org/10.1175/JPO-D-16-0270.1, 2017.

Everett, J. D., Baird, M. E., Oke, P. R., and Suthers, I. M.: An Avenue of Eddies: Quantifying the Biophysical Properties of Mesoscale Eddies in the Tasman Sea, Geophysical Research Letters, 39, https://doi.org/10.1029/2012GL053091, 2012.

Friedrich, T., Powell, B. S., Gunnarson, J. L., Liu, G., Giardina, S. F., Stuecker, M. F., Hošeková, L., Feloy, K., and Stock, C. A.: Submesoscale-Permitting Physical/Biogeochemical Future Projections for the Main Hawaiian Islands, Journal of Advances in Modeling Earth Systems, 16, e2023MS003 855, https://doi.org/10.1029/2023MS003855, 2024.

GEBCO Compilation Group: GEBCO 2023 Grid, https://doi.org/10.5285/f98b053b-0cbc-6c23-e053-6c86abc0af7b, 2023.

Gwyther, D. E.: dgwyther/seqom-analysis: analysis-scripts-v1, https://doi.org/10.5281/zenodo.19230574, software, 2026.

Gwyther, D. E., Kerry, C., Roughan, M., and Keating, S. R.: Observing System Simulation Experiments Reveal That Subsurface Temperature Observations Improve Estimates of Circulation and Heat Content in a Dynamic Western Boundary Current, Geoscientific Model Development, 15, 6541–6565, https://doi.org/10.5194/gmd-15-6541-2022, 2022.

Gwyther, D. E., Keating, S. R., Kerry, C., and Roughan, M.: How Does 4DVar Data Assimilation Affect the Vertical Representation of Mesoscale Eddies? A Case Study with Observing System Simulation Experiments (OSSEs) Using ROMS v3.9, Geoscientific Model Development, 16, 157–178, https://doi.org/10.5194/gmd-16-157-2023, 2023a.

Gwyther, D. E., Roughan, M., Kerry, C., and Keating, S. R.: Impact of Assimilating Repeated Subsurface Temperature Transects on State Estimates of a Western Boundary Current, Frontiers in Marine Science, 9, https://doi.org/10.3389/fmars.2022.1084784, 2023b.

Gwyther, D. E., Jeffers, M., and Bostock, H. C.: South-East Queensland Regional Ocean Model v1.7 rel 1.0 (SEQOM-1.7 v1.0), https://doi.org/10.5281/zenodo.19247625, software, 2026.

Huang, Z., Nichol, S. L., Harris, P. T., and Caley, M. J.: Classification of Submarine Canyons of the Australian Continental Margin, Marine Geology, 357, 362–383, https://doi.org/10.1016/j.margeo.2014.07.007, 2014.

IMOS: Argo Profiles - Core Data, 2025a.

IMOS: Gridded Sea Level Anomaly - Delayed Mode - DM02, 2025b.

IMOS: SST - L4 - RAMSSA - Australia, 2025c.

Janeković, I., Rayson, M. D., Jones, N. L., Watson, P., and Pattiaratchi, C.: 4D-Var Data Assimilation Using Satellite Sea Surface Temperature to Improve the Tidally-Driven Interior Ocean Dynamics Estimates in the Indo-Australian Basin, Ocean Modelling, 171, 101 969, https://doi.org/10.1016/j.ocemod.2022.101969, 2022.

Kerry, C. and Roughan, M.: Downstream Evolution of the East Australian Current System: Mean Flow, Seasonal, and Intra-annual Variability, Journal of Geophysical Research: Oceans, 125, e2019JC015 227, https://doi.org/10.1029/2019JC015227, 2020.

Kerry, C., Powell, B., Roughan, M., and Oke, P.: Development and Evaluation of a High-Resolution Reanalysis of the East Australian Current Region Using the Regional Ocean Modelling System (ROMS 3.4) and Incremental Strong-Constraint 4-Dimensional Variational (IS4D-Var) Data Assimilation, Geoscientific Model Development, 9, 3779–3801, https://doi.org/10.5194/gmd-9-3779-2016, 2016.

Kerry, C., Roughan, M., and Powell, B.: Predicting the Submesoscale Circulation Inshore of the East Australian Current, Journal of Marine Systems, 204, 103 286, https://doi.org/10.1016/j.jmarsys.2019.103286, 2020.

Kerry, C., Keating, S. R., Roughan, M., Azaneu, M., and Brassington, G. B.: Wide-Swath Satellite Altimetry Data Improves Modeled Mesoscale and Submesoscale Dynamics in a Western Boundary Current, Geophysical Research Letters, 53, e2025GL117 574, https://doi.org/10.1029/2025GL117574, 2026.

Kessouri, F., Bianchi, D., Renault, L., McWilliams, J. C., Frenzel, H., and Deutsch, C. A.: Submesoscale Currents Modulate the Seasonal Cycle of Nutrients and Productivity in the California Current System, Global Biogeochemical Cycles, 34, e2020GB006 578, https://doi.org/10.1029/2020GB006578, 2020.

Klein, P. and Lapeyre, G.: The Oceanic Vertical Pump Induced by Mesoscale and Submesoscale Turbulence, Annual Review of Marine Science, 1, 351–375, https://doi.org/10.1146/annurev.marine.010908.163704, 2009.

Klein, P., Hua, B. L., Lapeyre, G., Capet, X., Gentil, S. L., and Sasaki, H.: Upper Ocean Turbulence from High-Resolution 3D Simulations, Journal of Physical Oceanography, 38, 1748–1763, https://doi.org/10.1175/2007JPO3773.1, 2008.

Li, J., Roughan, M., and Kerry, C.: Dynamics of Interannual Eddy Kinetic Energy Modulations in a Western Boundary Current, Geophysical Research Letters, 48, e2021GL094 115, https://doi.org/10.1029/2021GL094115, 2021.

Li, J., Roughan, M., and Kerry, C.: Drivers of Ocean Warming in the Western Boundary Currents of the Southern Hemisphere, Nature Climate Change, 12, 901–909, https://doi.org/10.1038/s41558-022-01473-8, 2022.

Lin, H., Liu, Z., Hu, J., Menemenlis, D., and Huang, Y.: Characterizing Meso- to Submesoscale Features in the South China Sea, Progress in Oceanography, 188, 102 420, https://doi.org/10.1016/j.pocean.2020.102420, 2020.

Macdonald, H. S., Roughan, M., Baird, M. E., and Wilkin, J.: A Numerical Modeling Study of the East Australian Current Encircling and Overwashing a Warm-Core Eddy, Journal of Geophysical Research: Oceans, 118, 301–315, https://doi.org/10.1029/2012JC008386, 2013.

Malan, N., Archer, M., Roughan, M., Cetina-Heredia, P., Hemming, M., Rocha, C., Schaeffer, A., Suthers, I., and Queiroz, E.: Eddy-Driven Cross-Shelf Transport in the East Australian Current Separation Zone, Journal of Geophysical Research: Oceans, 125, e2019JC015 613, https://doi.org/10.1029/2019JC015613, 2020.

Malan, N., Roughan, M., Hemming, M., and Schaeffer, A.: Mesoscale Circulation Controls Chlorophyll Concentrations in the East Australian Current Separation Zone, Journal of Geophysical Research: Oceans, 128, e2022JC019 361, https://doi.org/10.1029/2022JC019361, 2023.

Mantovanelli, A., Keating, S., Wyatt, L. R., Roughan, M., and Schaeffer, A.: Lagrangian and Eulerian Characterization of Two Counter-Rotating Submesoscale Eddies in a Western Boundary Current, Journal of Geophysical Research: Oceans, 122, 4902–4921, https://doi.org/10.1002/2016JC011968, 2017.

Marchesiello, P., McWilliams, J. C., and Shchepetkin, A.: Open Boundary Conditions for Long-Term Integration of Regional Oceanic Models, Ocean Modelling, 3, 1–20, https://doi.org/10.1016/S1463-5003(00)00013-5, 2001.

McWilliams, J. C.: Submesoscale Currents in the Ocean, Proceedings of the Royal Society A: Mathematical, Physical and Engineering Sciences, 472, 20160 117, https://doi.org/10.1098/rspa.2016.0117, 2016.

McWilliams, J. C.: A Survey of Submesoscale Currents, Geoscience Letters, 6, 3, https://doi.org/10.1186/s40562-019-0133-3, 2019.

Mullaney, T. J. and Suthers, I. M.: Entrainment and Retention of the Coastal Larval Fish Assemblage by a Short-Lived, Submesoscale, Frontal Eddy of the East Australian Current, Limnology and Oceanography, 58, 1546–1556, https://doi.org/10.4319/lo.2013.58.5.1546, 2013.

Oke, P. R., Roughan, M., Cetina-Heredia, P., Pilo, G. S., Ridgway, K. R., Rykova, T., Archer, M. R., Coleman, R. C., Kerry, C. G., Rocha, C., Schaeffer, A., and Vitarelli, E.: Revisiting the Circulation of the East Australian Current: Its Path, Separation, and Eddy Field, Progress in Oceanography, 176, 102 139, https://doi.org/10.1016/j.pocean.2019.102139, 2019.

Onken, R., Baschek, B., and Angel-Benavides, I. M.: Very High-Resolution Modelling of Submesoscale Turbulent Patterns and Processes in the Baltic Sea, Ocean Science, 16, 657–684, https://doi.org/10.5194/os-16-657-2020, 2020.

Ridgway, K. R. and Dunn, J. R.: Mesoscale Structure of the Mean East Australian Current System and Its Relationship with Topography, Progress in Oceanography, 56, 189–222, https://doi.org/10.1016/S0079-6611(03)00004-1, 2003.

Rocha, C. B., Chereskin, T. K., Gille, S. T., and Menemenlis, D.: Mesoscale to Submesoscale Wavenumber Spectra in Drake Passage, Journal of Physical Oceanography, 46, 601–620, https://doi.org/10.1175/JPO-D-15-0087.1, 2016.

Sandery, P. A. and Sakov, P.: Ocean Forecasting of Mesoscale Features Can Deteriorate by Increasing Model Resolution towards the Submesoscale, Nature Communications, 8, 1566, https://doi.org/10.1038/s41467-017-01595-0, 2017.

Schaeffer, A., Gramoulle, A., Roughan, M., and Mantovanelli, A.: Characterizing Frontal Eddies along the East Australian Current from HF Radar Observations, Journal of Geophysical Research: Oceans, 122, 3964–3980, https://doi.org/10.1002/2016JC012171, 2017.

Shchepetkin, A. F. and McWilliams, J. C.: The Regional Oceanic Modeling System (ROMS): A Split-Explicit, Free-Surface, Topography-Following-Coordinate Oceanic Model, Ocean Modelling, 9, 347–404, https://doi.org/10.1016/j.ocemod.2004.08.002, 2005.

Sloyan, B. M., Cowley, R., and Chapman, C. C.: East Australian Current Velocity, Temperature and Salinity Data Products, Scientific Data, 11, 10, https://doi.org/10.1038/s41597-023-02857-x, 2024.

Sobral, F., Roughan, M., Malan, N., and Li, J.: Mean-State and Seasonal Variability in Temperature Structure and Heat Transport in the East Australian Current System From a Multi-Decadal Regional Ocean Model, Journal of Geophysical Research: Oceans, 129, e2023JC020 438, https://doi.org/10.1029/2023JC020438, 2024.

Sokolov, S. and Rintoul, S.: Circulation and Water Masses of the Southwest Pacific: WOCE Section P11, Papua New Guinea to Tasmania, Journal of Marine Research, 58, https://doi.org/10.1357/002224000321511151, 2000.

Song, Y. and Haidvogel, D.: A Semi-implicit Ocean Circulation Model Using a Generalized Topography-Following Coordinate System, Journal of Computational Physics, 115, 228–244, https://doi.org/10.1006/jcph.1994.1189, 1994.

Soufflet, Y., Marchesiello, P., Lemarié, F., Jouanno, J., Capet, X., Debreu, L., and Benshila, R.: On Effective Resolution in Ocean Models, Ocean Modelling, 98, 36–50, https://doi.org/10.1016/j.ocemod.2015.12.004, 2016.

Steven, A. D. L., Baird, M. E., Brinkman, R., Car, N. J., Cox, S. J., Herzfeld, M., Hodge, J., Jones, E., King, E., Margvelashvili, N., Robillot, C., Robson, B., Schroeder, T., Skerratt, J., Tickell, S., Tuteja, N., Wild-Allen, K., and Yu, J.: eReefs: An Operational Information System for Managing the Great Barrier Reef, Journal of Operational Oceanography, 12, S12–S28, https://doi.org/10.1080/1755876X.2019.1650589, 2019.

Su, C.-H., Torrance, J., Rennie, S., Howard, E., Stassen, C., Warren, R., Smith, A., Dharssi, I., Pepler, A., Tian, S., Lipson, M., Steinle, P., Franklin, C., Le, T., Wang, C., Masoumi, S., and Le Marshall, J.: The Australian Regional Atmospheric Reanalysis System, Version 2 – BARRA2, Journal of Southern Hemisphere Earth Systems Science, 75, ES25 032, https://doi.org/10.1071/ES25032, 2025.

Su, Z., Wang, J., Klein, P., Thompson, A. F., and Menemenlis, D.: Ocean Submesoscales as a Key Component of the Global Heat Budget, Nature Communications, 9, 775, https://doi.org/10.1038/s41467-018-02983-w, 2018.

https://doi.org/10.5194/egusphere-2026-1852
Preprint. Discussion started: 18 May 2026

Umlauf, L. and Burchard, H.: A Generic Length-Scale Equation for Geophysical Turbulence Models, Journal of Marine Research, 61, https://doi.org/10.1357/002224003322005087, 2003.

Wang, Y., Dong, J., Ji, C., and Dong, C.: Dependence of Submesoscale Simulation on Turbulence Closure Schemes in the Regional Ocean Modeling System (ROMS), Ocean Modelling, 180, 102 120, https://doi.org/10.1016/j.ocemod.2022.102120, 2022.

Wong, A. P. S., Wijffels, S. E., Riser, S. C., Pouliquen, S., Hosoda, S., Roemmich, D., Gilson, J., Johnson, G. C., Martini, K., Murphy, D. J., Scanderbeg, M., Bhaskar, T. V. S. U., Buck, J. J. H., Merceur, F., Carval, T., Maze, G., Cabanes, C., André, X., Poffa, N., Yashayaev, I., Barker, P. M., Guinehut, S., Belbéoch, M., Ignaszewski, M., Baringer, M. O., Schmid, C., Lyman, J. M., McTaggart, K. E., Purkey, S. G., Zilberman, N., Alkire, M. B., Swift, D., Owens, W. B., Jayne, S. R., Hersh, C., Robbins, P., West-Mack, D., Bahr, F., Yoshida, S., Sutton, P. J. H., Cancouët, R., Coatanoan, C., Dobbler, D., Juan, A. G., Gourrion, J., Kolodziejczyk, N., Bernard, V., Bourlès, B., Claustre, H., D'Ortenzio, F., Le Reste, S., Le Traon, P.-Y., Rannou, J.-P., Saout-Grit, C., Speich, S., Thierry, V., Verbrugge, N., Angel-Benavides, I. M., Klein, B., Notarstefano, G., Poulain, P.-M., Vélez-Belchí, P., Suga, T., Ando, K., Iwasaska, N., Kobayashi, T., Masuda, S., Oka, E., Sato, K., Nakamura, T., Sato, K., Takatsuki, Y., Yoshida, T., Cowley, R., Lovell, J. L., Oke, P. R., van Wijk, E. M., Carse, F., Donnelly, M., Gould, W. J., Gowers, K., King, B. A., Loch, S. G., Mowat, M., Turton, J., Rama Rao, E. P., Ravichandran, M., Freeland, H. J., Gaboury, I., Gilbert, D., Greenan, B. J. W., Ouellet, M., Ross, T., Tran, A., Dong, M., Liu, Z., Xu, J., Kang, K., Jo, H., Kim, S.-D., and Park, H.-M.: Argo Data 1999–2019: Two Million Temperature-Salinity Profiles and Subsurface Velocity Observations From a Global Array of Profiling Floats, Frontiers in Marine Science, 7, https://doi.org/10.3389/fmars.2020.00700, 2020.

Zhong, Y. and Bracco, A.: Submesoscale Impacts on Horizontal and Vertical Transport in the Gulf of Mexico, Journal of Geophysical Research: Oceans, 118, 5651–5668, https://doi.org/10.1002/jgrc.20402, 2013.

Zhou, Y., Duan, W., and Cheng, X.: Dynamics of Submesoscale Processes and Their Influence on Vertical Heat Transport in the Southeastern Tropical Indian Ocean, Ocean Dynamics, 74, 685–702, https://doi.org/10.1007/s10236-024-01628-5, 2024.